



# Spectroscopic Observations of Current Sheet Formation and Evolution

Harry P. Warren<sup>1</sup> , David H. Brooks<sup>2,3</sup> , Ignacio Ugarte-Urra<sup>1</sup> , Jeffrey W. Reep<sup>4</sup> ,  
Nicholas A. Crump<sup>1</sup>, and George A. Doschek<sup>1</sup>

<sup>1</sup> Space Science Division, Naval Research Laboratory, Washington, DC 20375, USA; [harry.warren@nrl.navy.mil](mailto:harry.warren@nrl.navy.mil)

<sup>2</sup> College of Science, George Mason University, 4400 University Drive, Fairfax, VA 22030 USA

<sup>3</sup> Hinode Team, ISAS/JAXA, 3-1-1 Yoshinodai, Chuo-ku, Sagami-hara, Kanagawa 252-5210, Japan

<sup>4</sup> National Research Council Postdoctoral Fellow, Space Science Division, Naval Research Laboratory, Washington, DC 20375, USA

Received 2017 November 29; revised 2018 January 20; accepted 2018 January 20; published 2018 February 20

## Abstract

We report on the structure and evolution of a current sheet that formed in the wake of an eruptive X8.3 flare observed at the west limb of the Sun on 2017 September 10. Using observations from the EUV Imaging Spectrometer (EIS) on *Hinode* and the Atmospheric Imaging Assembly (AIA) on the *Solar Dynamics Observatory*, we find that plasma in the current sheet reaches temperatures of about 20 MK and that the range of temperatures is relatively narrow. The highest temperatures occur at the base of the current sheet, in the region near the top of the post-flare loop arcade. The broadest high temperature line profiles, in contrast, occur at the largest observed heights. Furthermore, line broadening is strong very early in the flare and diminishes over time. The current sheet can be observed in the AIA 211 and 171 channels, which have a considerable contribution from thermal bremsstrahlung at flare temperatures. Comparisons of the emission measure in these channels with other EIS wavelengths and AIA channels dominated by Fe line emission indicate a coronal composition and suggest that the current sheet is formed by the heating of plasma already in the corona. Taken together, these observations suggest that some flare heating occurs in the current sheet, while additional energy is released as newly reconnected field lines relax and become more dipolar.

**Key words:** Sun: corona – Sun: flares

**Supporting material:** animation

## 1. Introduction

It is widely thought that eruptive solar flares are powered by the energy released during magnetic reconnection (e.g., Shibata et al. 1995). The standard thinking is that turbulent photospheric motions lead to the twisting and braiding of magnetic fields in the corona and that this topological complexity is ultimately dissipated through magnetic reconnection. The process of how energy stored in the magnetic field is transferred to the plasma, however, is poorly understood. For example, it is not clear if energy transport occurs through the formation of shocks from field lines retracting from the reconnection region, the acceleration of particles in the current sheet, the dissipation of waves, or through some combination of these, and perhaps other mechanisms. The lack of progress on these issues stems from the difficulty of observing magnetic reconnection directly. Theory suggests that it occurs on very small spatial scales (e.g., Zweibel & Yamada 2009). Furthermore, the plasma processed through the current sheet is from the relatively tenuous corona. This combination of small volumes and low densities should lead to a low emission measure and make it challenging to observe.

In this paper, we report on the structure and evolution of a current-sheet-like feature that formed in the wake of a solar eruption and flare that occurred on the west limb of the Sun on 2017 September 10. There is no commonly accepted observational signature of a current sheet, but, as we will see, this event has all of the expected features. The eruption begins with the heating of a filament low in the corona. As the filament erupts, it forms a cavity that expands as it moves outward. Bright, high temperature emission develops at the base of the eruption and eventually evolves into a classic post-flare loop arcade with a

cusplike shape at its top. Finally, a long, narrow, linear structure forms from the top of the cusp and follows the path of the erupting filament. It is this feature that we assume to be the current sheet where magnetic reconnection is occurring.

Here we discuss observations of the event from the EUV Imaging Spectrometer (EIS; Culhane et al. 2007) on *Hinode* (Kosugi et al. 2007) and the Atmospheric Imaging Assembly (AIA; Lemen et al. 2012) on the *Solar Dynamics Observatory* (SDO). At the time of the eruption, EIS was executing a flare watch study consisting of short exposures over a relatively wide field of view that extended up to about  $1.15 R_{\odot}$ . We use the ratio of the EIS Fe XXIV 255.10 Å to Fe XXIII 263.76 Å lines to infer temperatures of 15–20 MK in the current sheet. The highest temperatures occur near the base of the current sheet in the cusp-shaped feature at the top of the post-flare loop arcade and decline with height. Many previous studies had suggested elevated temperatures in this region relative to the brightest emission in the flare arcade (e.g., Tsuneta et al. 1997; Warren et al. 1999). Here we report the first temperature measurements that have extended into the current sheet just above the arcade. Comparisons with the AIA observations in this region indicate that the distribution of temperatures is relatively narrow, as it appears bright in the 193 and 131 channels that are dominated by high temperature emission lines and dim in the channels dominated by lower temperature lines. This is confirmed by a formal inversion of the observed intensities to compute the differential emission measure distribution.

Many previous studies of nonthermal line broadening in high temperature emission lines have utilized spatially unresolved observations (e.g., Doschek et al. 1980; Antonucci et al. 1984; Mariska et al. 1993). These studies have found that the largest

nonthermal velocities generally occur early in a flare, sometime even before any hard X-ray emission is detected (e.g., Alexander et al. 1998; Harra et al. 2001). We use spatially resolved observations of the EIS Fe XXIV 192.04 Å line to measure high temperature line broadening. We find that the strongest nonthermal velocities occur early in the flare, consistent with earlier results. Furthermore, we find that nonthermal broadening increases with height in the current sheet.

The current sheet can be observed in the AIA 211 and 171 channels, which do not have strong contributions from emission lines at flare temperatures (O’Dwyer et al. 2010). Thus the emission from the current sheet in these channels is likely to be from thermal bremsstrahlung. Comparisons with the emission from other EIS wavelengths and AIA channels dominated by Fe line emission can be used to infer elemental abundances. We find that the observations are consistent with a coronal composition in the current sheet.

Several previous eruptive flares have shown evidence for a current sheet, but such observations are relatively rare. Almost all previous spectroscopic observations appear to have been taken with the Ultraviolet Coronagraph Spectrometer (UVCS; Kohl et al. 1995) on the *Solar and Heliospheric Observatory* (*SoHO*). Ciaravella et al. (2002), Ko et al. (2003), Ciaravella & Raymond (2008), and Schettino et al. (2010) report on UVCS observations of four different events, all observed at heights above about  $1.5 R_{\odot}$ . Spectroscopic observations from EIS for one event observed at lower heights have been presented by Landi et al. (2012). Some spectroscopic observations from EIS near the base of the current sheet have been reported by Hara et al. (2008). The properties of long, thin current-sheet-like features have also been studied using imaging observations (e.g., Savage et al. 2010; Patsourakos & Vourlidis 2011; Reeves & Golub 2011; Hannah & Kontar 2013; Zhu et al. 2016; Seaton et al. 2017). Our results are generally consistent with these previous studies and we will discuss this in detail in the final section of the paper.

We also note that there are a number of papers in the literature that report on structures that are likely to be current sheets or at least closely related to them (e.g., Liu et al. 2013; Gou et al. 2015; Li et al. 2016). In observations such as these, the features of interest are short, linear structures that sit on top of the flare arcade, but whose intensity declines rapidly with height. There are also a number of events where diffuse, high temperature supra-arcade emission is evident (e.g., Savage et al. 2012; Kim et al. 2014; Guidoni et al. 2015; Chen et al. 2017; Reeves et al. 2017). The relationship of this type of emission to the current sheet, however, is less clear.

## 2. Observations

In this paper, we focus on the spatially resolved EIS and AIA observations of the 2017 September 10, X flare. We begin, however, with a discussion of some context soft-X-ray irradiance data from the X-ray Sensor (XRS; see, for example, Garcia 1994) on the *Geostationary Operational Environmental Satellite* (*GOES*). Light curves from the 1–8 and 0.5–4 Å channels are shown in Figure 1. The peak in the 1–8 channel occurred at 16:06:28 UT at a level of X8.3 ( $8.3 \times 10^4 \text{ W m}^{-2}$ ). The ratio of the two XRS channels can be used to infer a response-weighted average temperature (e.g., White et al. 2005). This analysis is also shown in Figure 1 and indicates a peak temperature of about 29 MK at 15:56:49. The

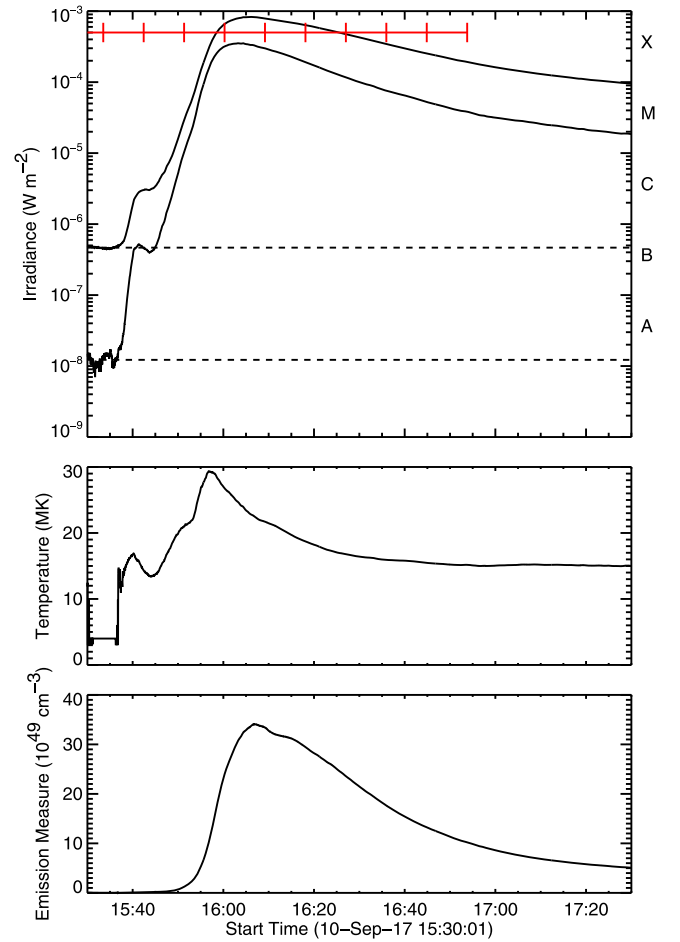


**Figure 1.** *GOES* soft-X-ray observations for the X8.3 flare that occurred on 2017 September 10 near 16 UT. *GOES* indicates the presence of relatively high temperature emission in the flare, but the spatial distribution of this hot plasma cannot be determined from these integrated observations. Top: *GOES* light curves for the 1–8 and 0.5–4 Å channels. Dashed lines indicate the assumed background levels. The red ticks at the top of the plot indicate the start and stop times for each of the EIS rasters taken during this period. Middle and bottom: the temperature and emission measure derived from the *GOES* 0.5–4 to 1–8 Å ratio.

spatial distribution of this hot plasma, however, cannot be determined from these integrated observations.

AIA is a set of multi-layer telescopes capable of imaging the Sun at high spatial resolution (0.6 pixels) and high cadence (typically 12 s). EUV images are available at 94, 131, 171, 193, 211, 304, and 335 Å. AIA images are also available at UV and visible wavelengths, but they are not used in this analysis. During a flare, exposure times for the EUV channels are generally reduced in an alternating long–short pattern. For this event, the exposure time for the 193 channel, for example, was consistently 2 s until 15:44:31, when the exposure time of alternating images was reduced to better accommodate the intense emission from the flare. Exposure times in 193 went as low as 4.9 ms. The exposure times in the other EUV channels were handled similarly, except for 171, which used a fixed exposure time throughout. For display purposes, we have created composite long–short images, which show the brightest parts of the flare from the short exposure and the fainter emission using the long exposure. Note that all of the AIA data presented here were downloaded from the Stanford JSOC and processed with the SolarSoftware (SSW; Freeland & Handy 1998) routine `aia_prep` using the default settings.

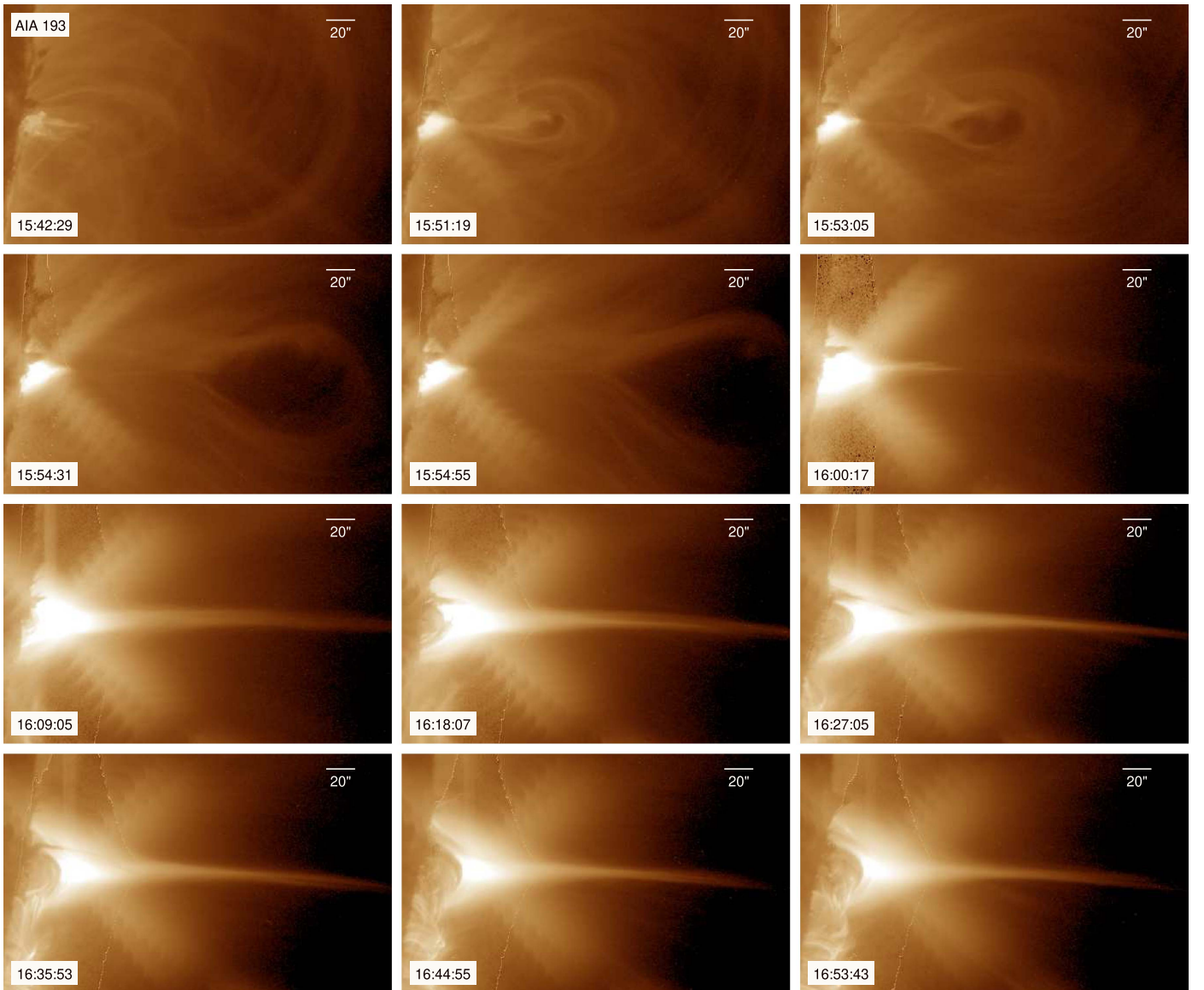


**Figure 2.** Series of AIA 193 Å images for the flare. This sequence shows the eruption of the filament and the formation of a linear, current-sheet-like feature behind the cavity. AIA 193 Å includes contributions from Fe XII and Fe XXIV and shows both the million degree corona and high temperature emission from the flare. The field of view shown here is  $268'' \times 166''$  centered at  $(1068'', -143'')$ . Note that these are composite images constructed from combining long and short exposure time images. The boundary between the two can be seen in many of the images. The wedge pattern seen in many of the images is the diffraction of emission from the brightest part of the flare off of the mesh supporting the front entrance filters.

Composite 193 images showing the eruption, post-flare loop arcade, and current sheet are presented in Figure 2. We note that the bright emission in the current sheet does not form simultaneously. Instead, the increase in intensity begins at the lowest heights and propagates outward between approximately 16:00 and 16:10 UT. To quantify this evolution, we have created a height-time plot of the intensity in a narrow region parallel to the current sheet. This is shown in Figure 3, and yields a speed of about  $288 \text{ km s}^{-1}$  for the propagation of the intensity radially along the current sheet.

One instrumental artifact that is worthy of mention here is the scattering of incident photons off of the mesh used to support the Al filters (see, for example, Poduval et al. 2013 and Lin et al. 2001). These filters are needed to block visible light from reaching the detector but also must be very thin to allow for EUV emission to pass. To increase their durability, they are supported by a thin mesh. This diffraction can be seen as the

wedge pattern emanating from the brightest emission in Figure 2. As we will see, EIS has a similar design and also shows this effect. The impact of this scattering on the observations will be discussed in the Appendix.

EIS is a high spatial and spectral resolution imaging spectrograph. EIS observes two wavelength ranges, 171–212 Å and 245–291 Å, with a spectral resolution of about 22 mÅ and a spatial pixel size of about  $1''$ . Solar images can be made by stepping the slit over a region of the Sun and taking an exposure at each position. Because of telemetry constraints, EIS is often restricted to saving only narrow spectral windows from each exposure. This restriction becomes particularly severe when high cadence is desired. Fortunately, for this event EIS received additional telemetry and was able to continuously run an observing sequence that saved 15 spectral windows over a field of  $240'' \times 304''$  using the  $2''$  slit and  $3''$  steps between exposures. The exposure time at each position was fixed at 5 s and the total



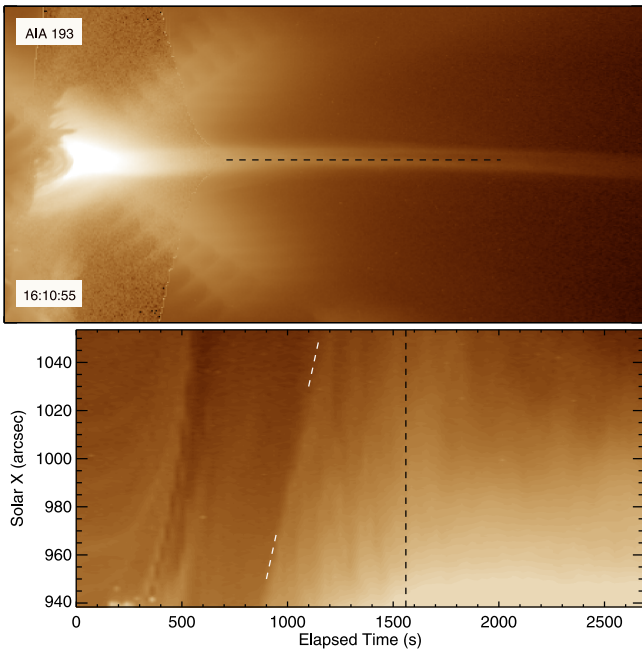


**Figure 3.** Bottom: the height-time plot of intensity along the current sheet showing how it brightens with time. The dashed white line corresponds to a velocity of  $0''.4 \text{ s}^{-1}$ , or  $288 \text{ km s}^{-1}$ , and represents the speed at which the intensity brightening propagates radially along the current sheet. Top: an example AIA 193 image showing the position of the “slit.” The time for this image is indicated by the black vertical line in the bottom panel.

(An animation of this figure is available.)

time for each raster was 535 s. The sequence used to observe this flare began at 05:44 on 2017 September 10, and ended at 16:53 UT, just after the peak of the event. Observations resumed at 18:33 in a “flare hunting” mode, where EIS executed a very low telemetry study until a flare was detected by the *Hinode* X-ray Telescope (XRT; Golub et al. 2007) and then branched to the high telemetry raster. These observations from late in the flare will be discussed in a separate paper.

All of the EIS level0 data from this time were processed using `eis_prep` with the default settings. We fit each spectral feature of interest in each raster with a Gaussian. There are approximately 30 emission lines available in these observations. Of primary interest here are Fe XXIV 192.04 Å, 255.10 Å, and Fe XXIII 263.76 Å. As we will show, the temperatures in the current sheet are relatively high and the current sheet is not observed in the lower temperature emission lines, such as Ca XVII 192.858 Å.

Since the exposure time is fixed, the brightest features near the peak of the flare are saturated. This is common for the Fe XXIV 192.04 Å line, which occurs near the peak effective area for EIS. The effective area is smaller in the long wavelength channel and the Fe XXIV 255.10 Å and Fe XXIII 263.76 Å lines are less affected by saturation. All of the EIS rasters in the Fe XXIV 255.10 Å line from near the peak of the flare are displayed in Figure 4.

### 2.1. Current Sheet Temperature

We now turn to a discussion of the temperature structure of the current sheet. The ratio of the Fe XXIV 255.10 Å to Fe XXIII 263.76 Å emission lines observed by EIS provides good sensitivity to temperature in the 6 to 22 MK range. This is

illustrated in Figure 5, where we show the theoretical ratio computed using CHIANTI v8.0.2 (Dere et al. 1997; Del Zanna et al. 2015).

Figure 6 shows the value of this ratio over the EIS field of view for three different times during the flare. In each case, the peak ratio, and therefore the peak temperature, occurs at intermediate heights, essentially in the cusp region above the brightest emission in the flare. The temperature declines with height above the limb in the current sheet. This is clearly seen in the lower panels of Figure 6, which show the intensity, ratio, and temperature as functions of height in the current sheet. In each case, the temperature of the brightest emission in the flare arcade is about 12 MK, rises to 20–25 MK just above this region, and then slowly declines back to about 12 MK at the largest heights for which the ratio can be measured. Saturation affects the brightest emission early in the flare. We can, however, infer the temperature in this region by examining the diffracted signal, which shows ratios in the brightest region of the flare of approximately 2–3. This corresponds to temperatures of 12–14 MK.

There are significant limitations to using a single pair of emission lines to infer a temperature. It does not, for example, yield any information on the distribution of temperatures. Fortunately, the AIA EUV channels are also sensitive to high temperature flare emission and we can combine the EIS and AIA observations to compute a well constrained temperature distribution.

A detailed discussion of the AIA temperature response is given by O’Dwyer et al. (2010). Briefly, at temperatures above 10 MK the 193 channel is dominated by Fe XXIV 192.04 Å (which peaks at  $\log T = 7.25$ ), 131 by Fe XXI 128.75 Å (7.05), and 94 by Fe XVIII 93.93 Å (6.85). At flare temperatures, the 335 channel is affected by crosstalk from the 131 channel and has a significant contribution from Fe XXI 128.75 Å (see Boerner et al. 2012 Section 2.2). The 211 and 171 channels do not have a significant contribution from emission lines formed above 10 MK and instead are dominated by continuum emission at these temperatures. As will be discussed in the next subsection, we can exploit this to infer the composition in the current sheet.

A set of AIA EUV images taken near 16:41:50 UT is shown in Figure 7. The current sheet is bright in 193 and 131 but faint in 94, suggesting that the distribution of temperatures is relatively narrow, as there does not appear to be much emission from Fe XVIII. To quantify this further, we investigate the emission measure structure implied by the EIS and AIA observations.

While the current sheet is clearly evident in the AIA images, there is still a contribution from foreground and background emission from the million degree corona in these channels. To subtract this contribution, we have taken slices across the current sheet and fit the resulting intensities with a combination of a Gaussian and second-order polynomial. The peak of the Gaussian is taken as the intensity in the current sheet at that height. This is illustrated in Figure 8, where we show the intensities for a single slice across the current sheet. We have also done this with the emission in the EIS channels. The EIS Fe XXIV and Fe XXIII emission lines are not affected by foreground or background emission. They are, however, affected by the diffracted signal from the mesh. This is about a 10% effect for both lines at the lowest heights, and the diffracted signal becomes smaller with height.

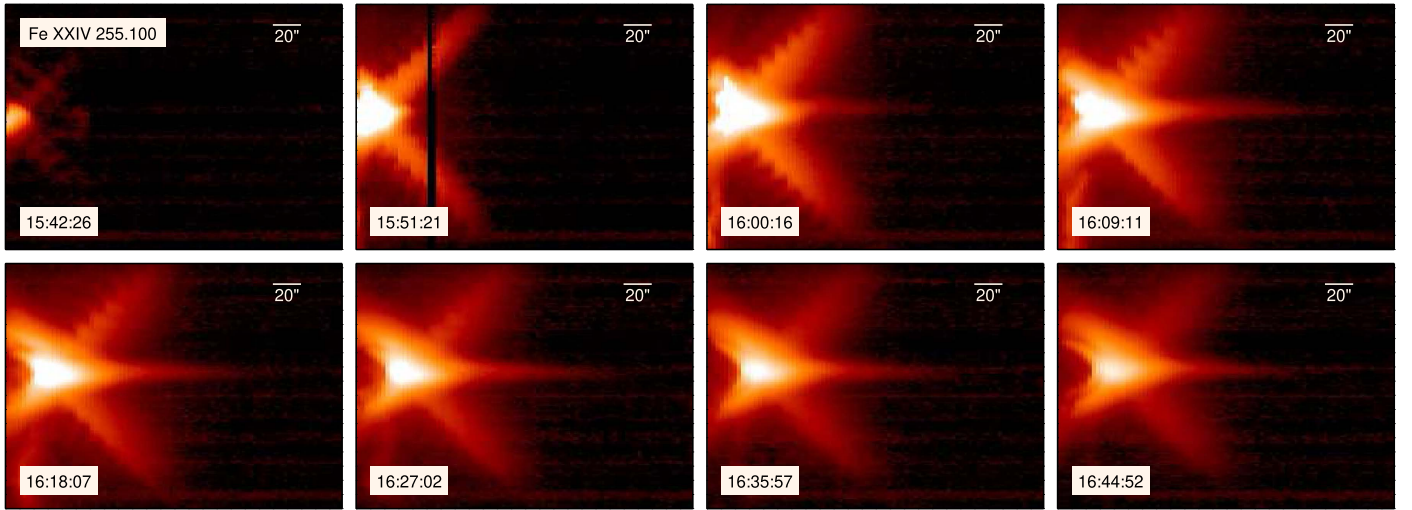


**Figure 4.** Time series of EIS Fe XXIV 255.10 Å rasters. The field of view shown here is  $240'' \times 174''$  centered at  $(1069'', -138'')$ . Note that some of the brightest pixels early in the flare are saturated. As with the AIA images, the wedge pattern seen in many of the rasters is the diffraction of the brightest part of the flare off of the mesh supporting the front entrance filters.

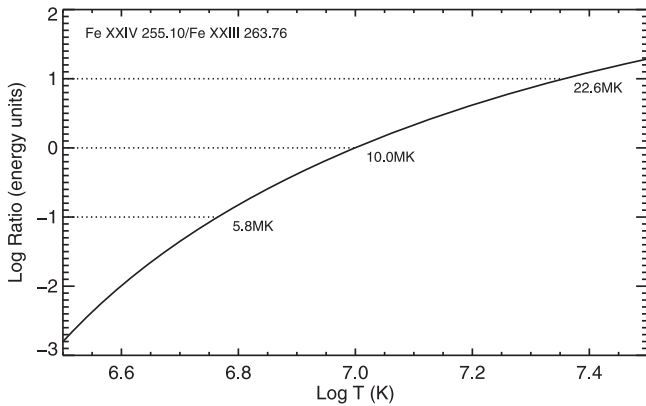


**Figure 5.** Theoretical ratio of Fe XXIV 255.10 Å to Fe XXIII 263.76 Å as a function of temperature computed using the CHIANTI ionization fractions. The temperatures corresponding to ratios of 0.1, 1, and 10 are highlighted.

The intensities can be used to compute emission measure loci curves,

$$\text{EM}(T) = \frac{I_{\text{obs}}}{\epsilon_{\lambda}(T)}, \quad (1)$$

where  $I_{\text{obs}}$  is an observed intensity and  $\epsilon_{\lambda}(T)$  is the corresponding emissivity or temperature response curve. These curves form an envelope on the emission measure distribution and are useful for investigating the temperature structure of the plasma without performing a formal inversion. For the AIA channels, we use the SSW routine `aia_get_response` with the “evenorm” and “timedepend” options to compute the temperature responses and to correct for the decline in sensitivity over the mission. To bring the EIS Fe XXIV 255.10 Å into agreement with AIA 193, we multiply the intensities of the EIS long wavelength lines by a factor of 1.8 (see Del Zanna 2013 and Warren et al. 2014 for a discussion of the EIS calibration). An example set of EM loci curves is also shown in Figure 8. The general confluence of curves near a temperature of 16 MK suggests a relatively narrow temperature

distribution, consistent with the simple interpretation of the raw images. The largest discrepancy is for the 335 channel, the origin of which is unclear. Interpreting the emission from this channel has proven problematic in a number of different analyses (see, for example, Boerner et al. 2014).

Finally, it is possible to use the intensities to perform a formal inversion and estimate the differential emission measure distribution (DEM). For this, we use the “MCMC” method as described by Kashyap & Drake (1998). This is a Bayesian method that assumes no functional form for the DEM. It also provides estimates of the error in the DEM by recalculating the emission measure using perturbed values for the intensities. The resulting calculation is also shown in Figure 8 and confirms the narrow distribution inferred from the images. With the exception of the AIA 335 channel, the agreement between the observed intensities and those computed from the DEM are generally within 25%. Intensities computed from the DEM shown in Figure 8 are given in Table 1.

We have computed background subtracted intensities, emission measure loci curves, and DEMs for a number of times and positions in the flare. The resulting temperatures are consistent with those derived from the simple EIS Fe XXIV to Fe XXIII ratio and the more detailed analysis from Figure 8. The measured temperatures are always approximately 15–20 MK and the temperature distributions are always narrow.

It is important to remember that this temperature analysis is predicated on the assumption that the plasma is in ionization equilibrium. Since the emission from the current sheet is relatively faint relative to the rest of the flare, the densities are relatively low and this assumption could be invalid. Shen et al. (2013) compared simulated intensities from equilibrium and nonequilibrium calculations and found differences of about a factor of 2. The magnitude of these effects depends inversely on density. For this event, if we take the isothermal emission measure and assume that the depth of the current sheet is equal to its measured full width at half maximum ( $2.355\sigma \sim 10''6$ ), we obtain a density of about  $n_e \sim (10^{29.6}/10^{8.9})^{1/2} \sim 10^{10} \text{ cm}^{-3}$  (see Figure 8), much larger than the density considered by Shen et al. (2013), which suggests that nonequilibrium effects are likely to be much smaller. This is just an upper bound on the

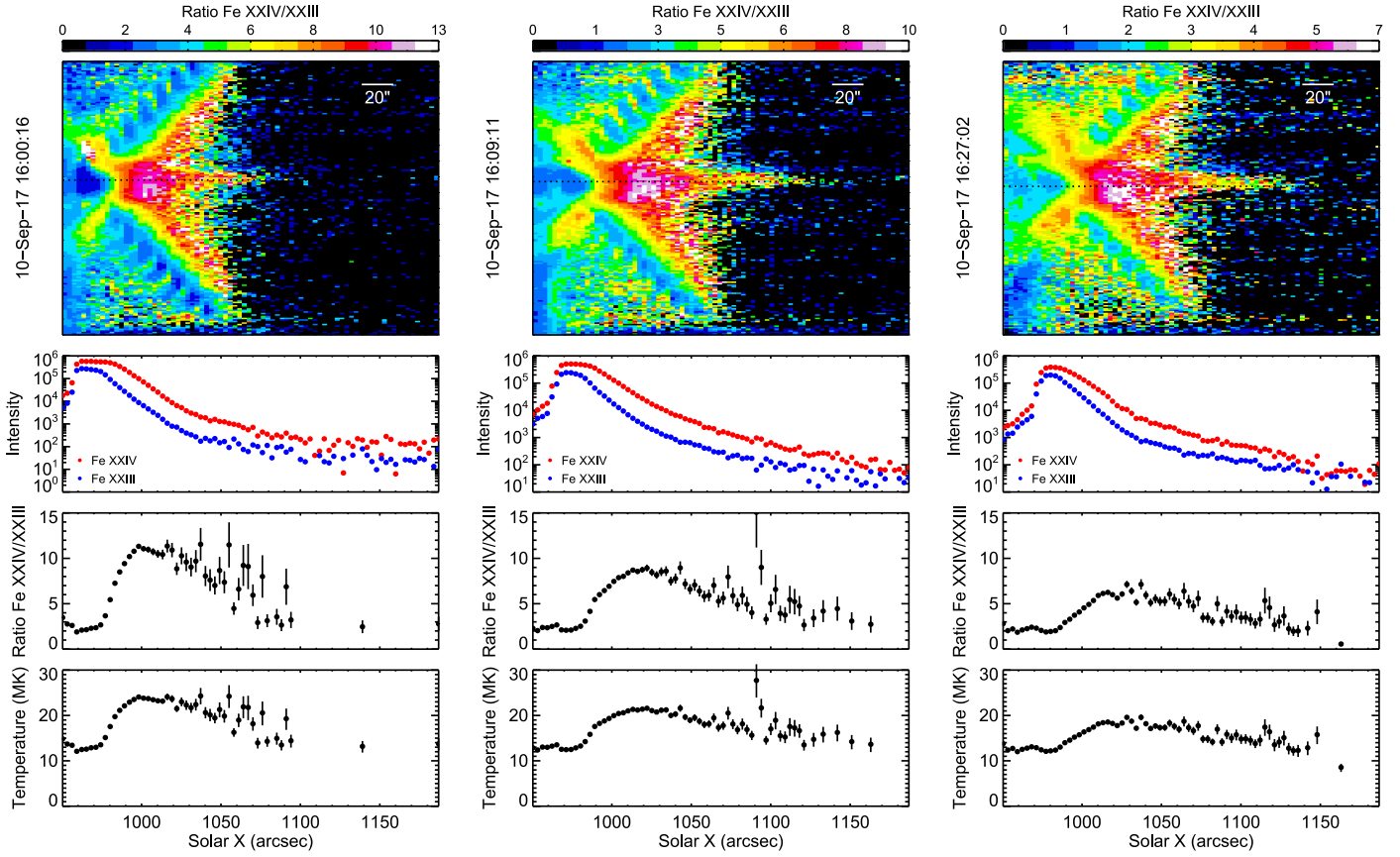


**Figure 6.** Temperature in the flare arcade and current sheet as a function of space and time as determined from the EIS Fe XXIV/Fe XXIII ratio. The temperature peaks at the base of the current sheet and declines with height. The highest temperatures are observed early in the event. Note that the color scale is different for each ratio map to emphasize the relative differences in temperature observed at that time. The intensity, Fe XXIV/Fe XXIII ratio, and derived temperatures along the dotted line tracing the current sheet are shown in the lower panels.

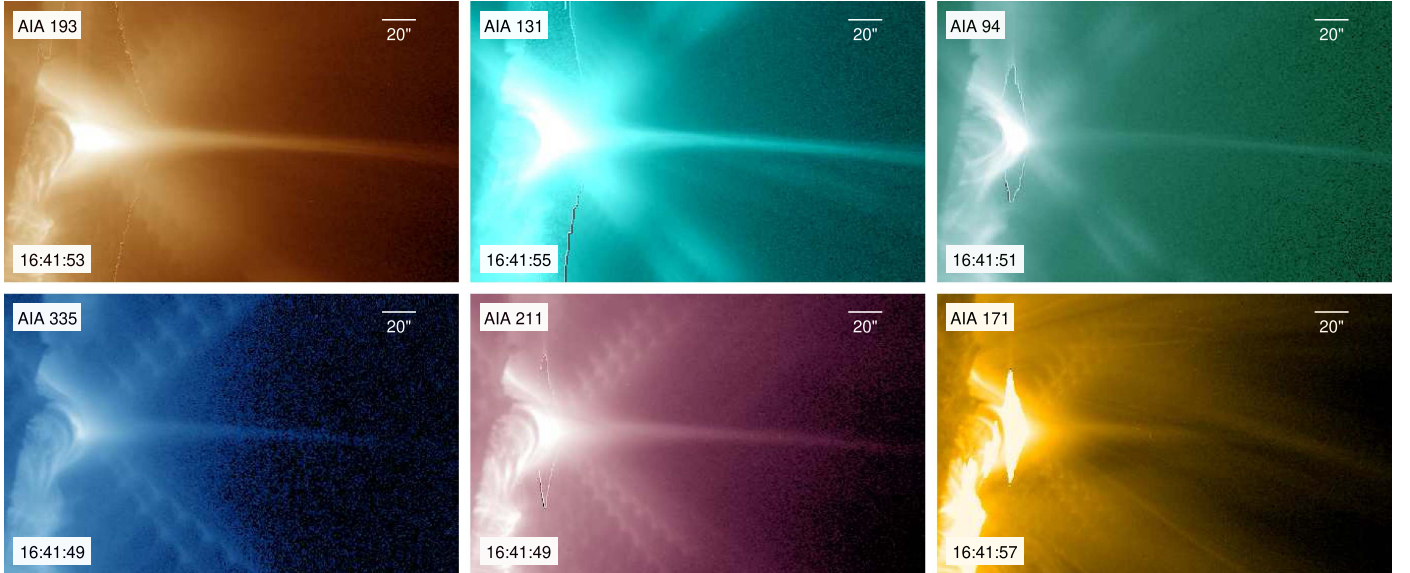


**Figure 7.** AIA images near 16:41:50 UT. The current sheet is bright in 193 (Fe XXIV) and 131 (Fe XXI) but relatively weak in 94 (Fe XVIII). This suggests that the temperature in the current sheet is relatively high (10–20 MK) and that the distribution of temperatures is relatively narrow. Despite the absence of high temperature line emission in the 211 and 171 channels, there is some evidence of the current sheet at these wavelengths. As discussed in the text, this appears to be from continuum emission.

density, but the depth of the current sheet is ultimately limited by the length of the flare ribbon and this estimate cannot be too far off.

## 2.2. Current Sheet Abundances

Measurements of elemental abundances hold potential clues to how plasma in the solar atmosphere is heated. It is now



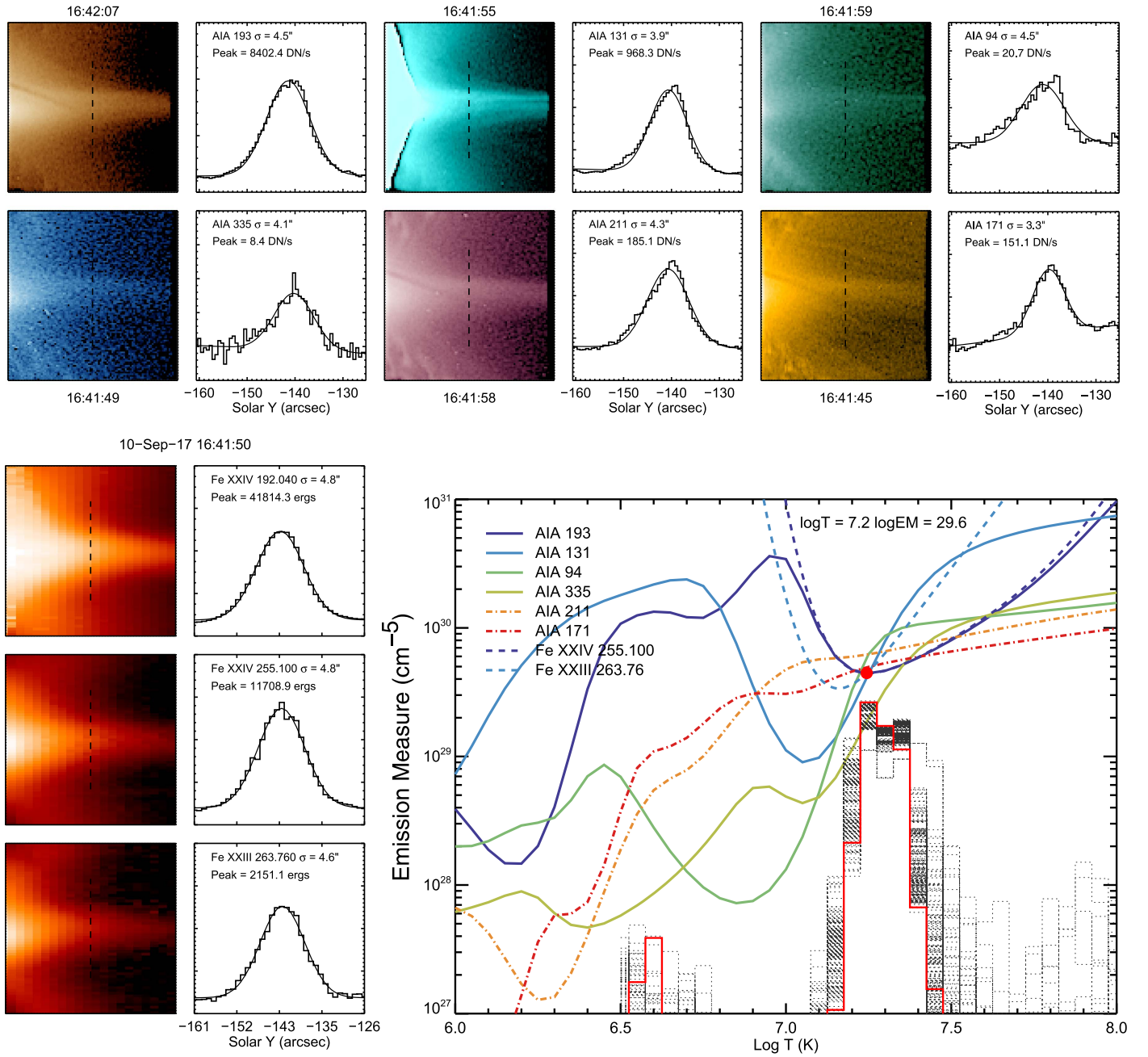


**Figure 8.** Emission measure analysis of the current sheet observed by EIS and AIA near 16:41:50 UT at a position of  $(1028'', -143'')$ . The observed intensities are approximately consistent with an isothermal temperature of about 16 MK, as indicated by the red dot. An MCMC emission measure inversion (red line) is also consistent with a narrow temperature distribution. Also shown are 250 Monte Carlo MCMC calculations (thin black lines). The paired panels each show a  $60'' \times 60''$  region near the base of the current sheet and the intensities along a slice perpendicular to the current sheet. Intensities used in the emission measure analysis are derived from the peak of a Gaussian fit to data along the slice.

recognized that elemental abundances are not fixed but vary from feature to feature and that these variations are organized by first ionization potential (FIP; for a review see Laming 2015). There is some evidence that high temperature flare emission has essentially a photospheric abundance (e.g., Warren 2014), suggesting that this plasma originates deep in the chromosphere and is evaporated into the corona before it has time to fractionate. Other studies indicate that the composition in flares can be complex, sometimes showing a photospheric composition, but other times showing FIP enhancements or even an inverse FIP effect (see Doschek et al. 2015 and Doschek & Warren 2017 and references therein).

As mentioned previously, the AIA 211 and 171 channels do not include strong emission lines formed at temperatures above 10 MK. As can be seen in Figures 7 and 8, however, the current sheet can be seen at these wavelengths. This is likely to be from continuum emission at these wavelengths (see O'Dwyer et al. 2010), which makes the magnitude of the intensities measured in these channels independent of the Fe abundance. We have recalculated the AIA temperature response curves, assuming a photospheric composition and confirmed this. The other EIS wavelengths and AIA channels dominated by line emission scale linearly with the Fe abundance. The response curves shown in Figure 8 are all computed assuming a coronal

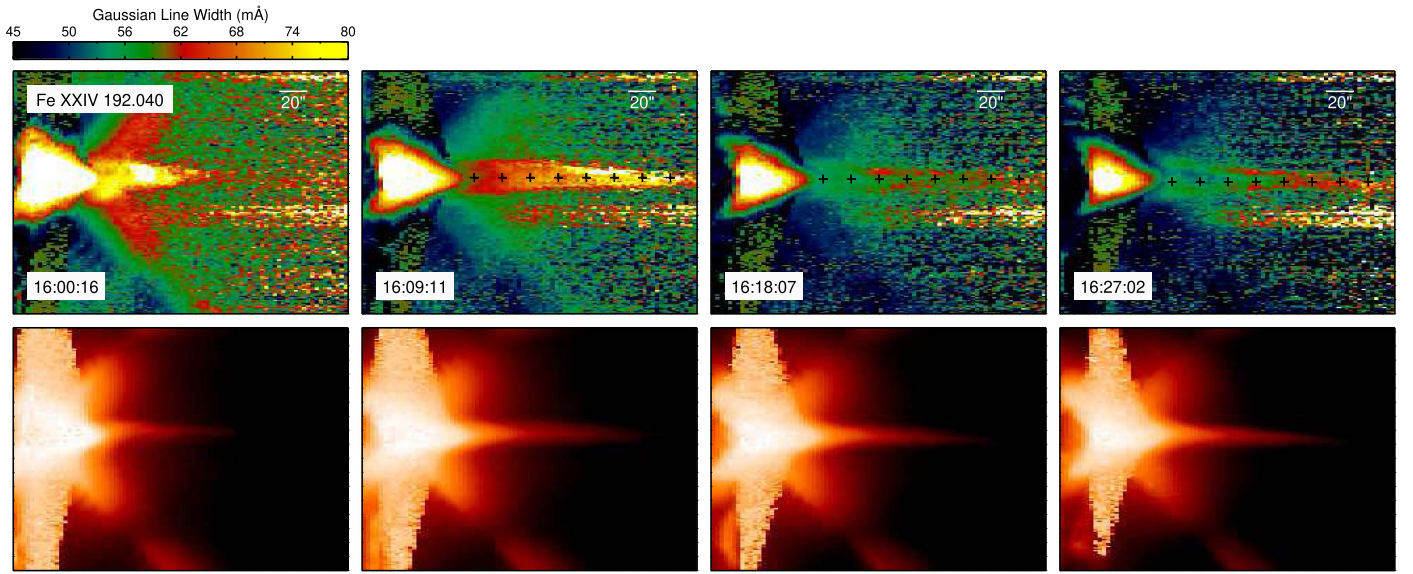


**Figure 9.** Line widths and intensities derived from the EIS Fe XXIV 192.04 Å line. The field of view shown here is  $240'' \times 174''$  centered at  $(1069'', -138'')$ . The broadest profiles tend to occur early in the event and broadening appears to increase with height above the arcade. Line widths also decrease with time during the event. Nonthermal velocity calculations at selected positions (marked by the crosses) are shown in Figure 10.

**Table 1**  
Observed and Computed Intensities<sup>a</sup>

Line	Inst	$I_{\text{obs}}$	$I_{\text{dem}}$	Ratio	Used
Fe XXIV 255.10	EIS	21076.0	26198.0	0.80	Y
Fe XXIII 263.76	EIS	3871.9	4003.7	0.97	Y
193	AIA	8402.4	9588.1	0.88	Y
131	AIA	968.3	1352.3	0.72	Y
94	AIA	20.7	27.7	0.75	Y
335	AIA	8.4	72.1	0.12	N
211	AIA	185.1	228.8	0.81	Y
171	AIA	151.1	177.3	0.85	Y

**Note.**

<sup>a</sup> Observed and computed intensities for the DEM analysis displayed in Figure 8. Intensities are in units of  $\text{erg cm}^{-2} \text{s}^{-1} \text{sr}^{-1}$  for EIS and  $\text{DN s}^{-1}$  for AIA. The ratios correspond to  $I_{\text{obs}}/I_{\text{dem}}$ . The “Used” column indicates if a line has been used to compute the DEM.

composition (Feldman et al. 1992), where the low FIP elements are enriched by about a factor of 4 over their photospheric values. The fact that the AIA 211 and 171 emission measure loci curves nearly coincide with those from the other channels around 16 MK when coronal abundances are used indicates that the composition in the current sheet is close to coronal.

### 2.3. Current Sheet Turbulence

We now turn to the measurement of nonthermal velocities in the current sheet. For this, we consider Fe XXIV 192.04 Å. The EIS effective area is relatively high at this wavelength and the line can generally be measured at the largest heights observed in the raster. Maps of the Gaussian line width at several times during the flare are shown in Figure 9. These maps clearly show that the widest profiles are observed early in the flare, that the line widths appear to increase with height above the limb in the current sheet, and that the line broadening diminishes with time during the event.

The observed line width results from a combination of thermal broadening, instrumental broadening, and nonthermal

turbulent motions of the plasma. This can be expressed as

$$W_{\text{obs}}^2 = W_{\text{inst}}^2 + 4 \ln(2) \left( \frac{\lambda}{c} \right)^2 (v_T^2 + v_{\text{NT}}^2), \quad (2)$$

where  $\lambda$  is the wavelength of the emission,  $c$  is the speed of light, and  $v_T^2 = 2k_B T/M$  is the thermal velocity, where  $k_B$  is the Boltzmann constant,  $T$  is the temperature, and  $M$  is the ion mass, and  $v_{\text{NT}}$  is the nonthermal velocity. To account for the temperature dependence in the calculation, we use the temperatures derived from the Fe XXIV to the Fe XXIII ratio shown in Figure 6. Since the temperatures are somewhat noisy, we use values interpolated from a simple exponential fit to the observed temperature profiles.

Nonthermal velocity calculations are presented in Figures 10 and 11 for eight positions along the current sheet observed in the 16:09, 16:18, and 16:27 UT rasters. The combination of increasing observed line width and declining temperature lead to a significant rise in the nonthermal velocity with height in the current sheet. In the 16:09 UT raster, for example, we see a rise from about  $87 \text{ km s}^{-1}$  to about  $152 \text{ km s}^{-1}$  over the observed length of the current sheet. At the other times, the nonthermal velocities are reduced, but not as much as is suggested in the maps of the line widths. Since the temperature is also declining with time, the nonthermal velocity does not vanish over this period. In the 16:27 UT raster, for example, the values are  $73 \text{ km s}^{-1}$  and  $101 \text{ km s}^{-1}$  at the lowest and highest heights, respectively.

### 3. Summary

We have presented an analysis of the current sheet observed during the 2017 September 10, X8.3 flare with EIS and AIA. This analysis shows that, while the temperature in the current sheet is much higher than that of the surrounding corona, the highest temperatures are observed in the cusp of the flare arcade and the temperature in the current sheet declines with height. We find that the distribution of temperatures in the current sheet is relatively narrow and is locally well described



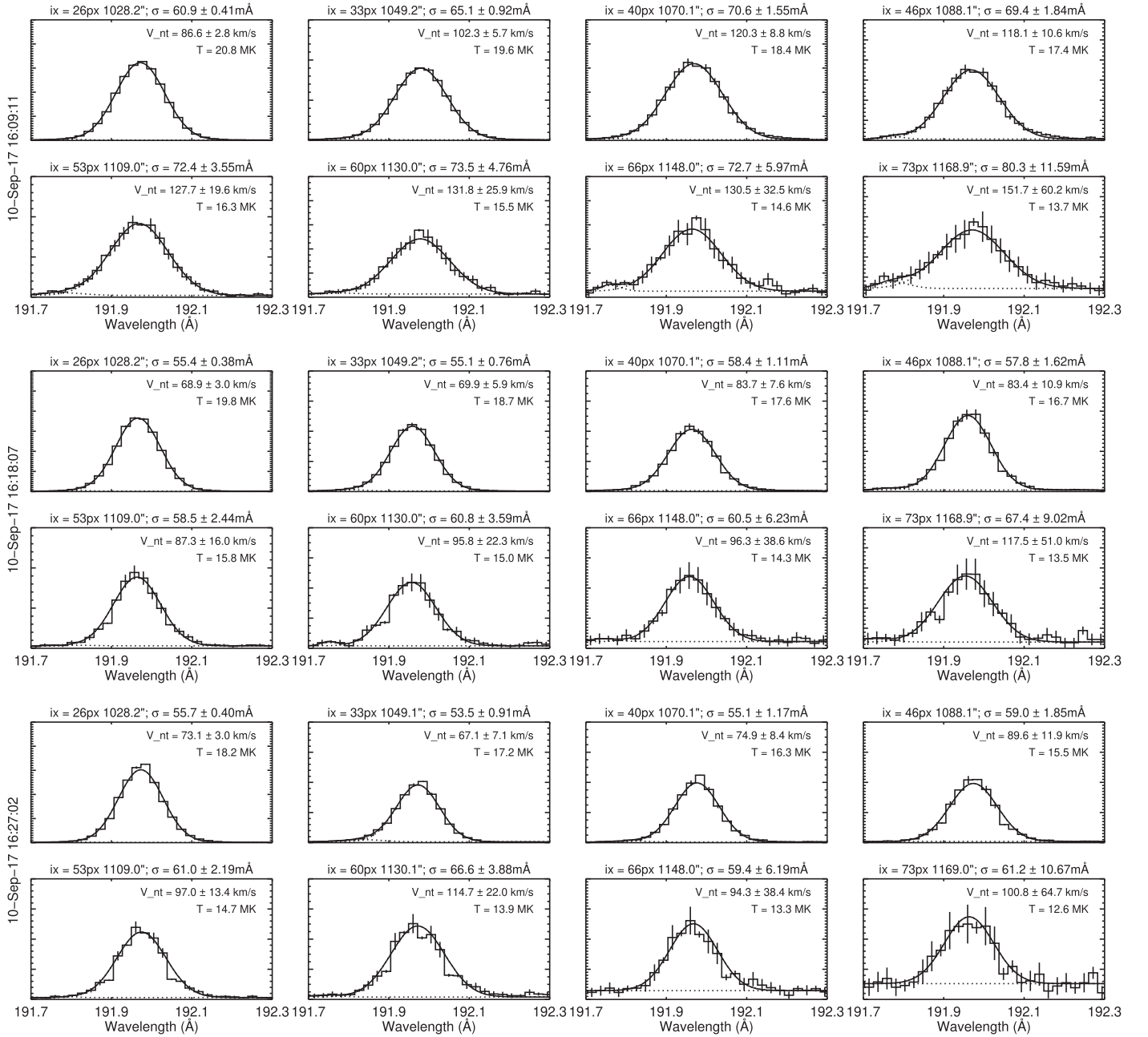


**Figure 10.** EIS Fe XXIV 192.04 Å line profiles and nonthermal velocities as a function of height for various times during the early part of the event. The observed Gaussian width, observed temperature, and the inferred nonthermal velocity for each profile is indicated in each panel. The EIS instrumental width (FWHM) is approximately 70.4 mÅ at this position.

as an isothermal plasma with a temperature of 15–20 MK. Furthermore, the observations show that the intensity enhancement in the current sheet begins at the lowest heights and propagates outward at a speed of about  $288 \text{ km s}^{-1}$ .

The spatial dependence of the temperature in the flare arcade suggests that some heating occurs in the current sheet itself, but that additional energy must be released after the field has reconnected. One possibility is that energy is released as field lines relax and become more dipolar after reconnection. This process has been well observed (e.g., Forbes & Acton 1996; McKenzie & Hudson 1999; Reeves et al. 2008a, 2008b; Savage & McKenzie 2011; Imada et al. 2013) and there is some indication that it leads to significant energy release (e.g.,

Guidoni & Longcope 2011; Hanneman & Reeves 2014; Scott et al. 2016). Of course, energetic particle acceleration is also likely to play a role in energy transport during this time.

The observed intensities in the AIA 211 and 171 channels, which do not have significant contributions from high temperature line emission, are consistent with a coronal composition. This suggests a coronal source for the plasma in the current sheet. This is consistent with the observations of very high temperature flare plasma observed at soft X-ray wavelengths (Caspi & Lin 2010).

Finally, we observe strong nonthermal broadening of approximately  $70\text{--}150 \text{ km s}^{-1}$  in the current sheet. This broadening increases with height above the limb and declines

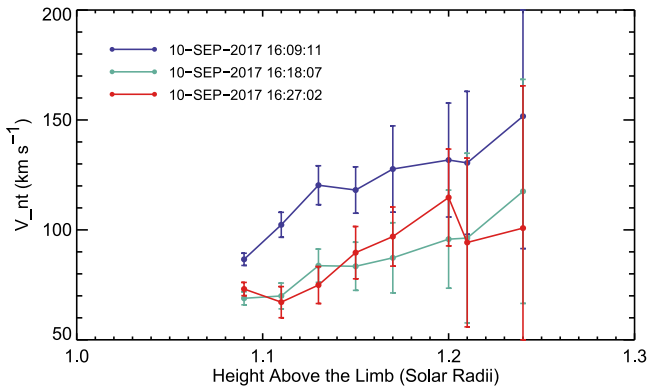


**Figure 11.** A summary of the EIS Fe XXIV 192.04 Å nonthermal velocities as a function of height presented in Figure 10.

with time. This is generally consistent with the previous observations of nonthermal velocities in flares (e.g., Doschek et al. 1980; Antonucci et al. 1984; Mariska et al. 1993); though, these spatially unresolved measurements are likely to have been dominated by the brightest emission. Our results are also consistent with the trend of increasing broadening with height observed in previous EIS observations of high temperature emission just above the flare arcade (Hara et al. 2008; Doschek et al. 2014).

Observations of current sheets have been presented previously in the literature. Ciaravella et al. (2002), Ko et al. (2003), Ciaravella & Raymond (2008), and Schettino et al. (2010) have all reported on the properties of linear structures that form in the wake of a coronal mass ejection as observed by UVCS. Despite observing the current sheet at much larger heights and generally much later in the event than we have, their results are largely consistent with what we observe here. Each of the studies finds evidence for high temperature emission, as Fe XVIII, Si XII, and Ca XIV are detected. Their temperatures, however, are generally lower than what we report here for the region just above the flare arcade. Ciaravella et al. (2002), Ko et al. (2003), and Ciaravella & Raymond (2008) all report FIP enhancements of varying magnitudes in the current sheet. Schettino et al. (2010) and Ciaravella & Raymond (2008) report strong broadening in the Fe XVIII line. Interestingly, of the existing spectroscopic observations, those reported by Landi et al. (2012) for EIS observations relatively close to the limb ( $\sim 1.1 R_{\odot}$ ), should be the closest to what we have presented, but their results are perhaps the least similar. In contrast to what we have found, Landi et al. (2012) find that the temperature in the current sheet never exceeds 3 MK and that the current sheet densities are comparable to the background emission. Landi et al. (2012) do find a coronal composition and enhanced line widths in the current sheet, consistent with our findings. This eruption was from an occulted active region and the EIS observations are likely to be at a larger height than suggested by the position of the slit. The event also did not produce a signature in GOES and may have been much less energetic.

As mentioned in the Introduction, there have been several imaging observations of current sheets with AIA/SDO and XRT/Hinode. The C4.9 event of 2010 November 3 (Reeves & Golub 2011; Hannah & Kontar 2013) is perhaps the most similar morphologically to what we have observed, with a narrow linear feature connecting the ejecta and the post-flare loop arcade. AIA DEM analysis for that flare indicates similar

10–20 MK temperatures in the current sheet (Hannah & Kontar 2013). The current sheets analyzed by Zhu et al. (2016) and Seaton et al. (2017) also have similar, but somewhat lower, temperatures to what we measure in the 2017 September 10 flare, but these current sheets are considerably fainter relative to the background emission. The flare analyzed by Zhu et al. (2016) was a C2.0 event, while the flare analyzed by Seaton et al. (2017) was an X4.9 event.

Magnetic reconnection is widely believed to play a major role in all flaring activity and thus extended current sheets should be present in all coronal mass ejections. It is curious then that the literature on the physical properties of current sheets is so sparse. As mentioned in the Introduction, the obvious argument is that the current sheet should be thin and relatively tenuous and thus have a low emission measure. Our observations, however, show a current sheet that has a high emission measure and is relatively thick. In Figure 8, we see an isothermal emission measure of approximately  $10^{30} \text{ cm}^{-5}$ , orders of magnitude higher than the background corona (e.g., Warren & Brooks 2009). Figure 8 also shows an observed width of over 3000 km for both EIS and AIA, much larger than the spatial resolution of either instrument (see Brooks et al. 2012 for measurements of loops observed with EIS and AIA). The AIA studies mentioned in the previous paragraph also show relatively wide current sheets when they are observed. This suggests that significant heating in the current sheet may only occur under very specific conditions.

This work was supported by NASA’s *Hinode* project. *Hinode* is a Japanese mission developed and launched by ISAS/JAXA, with NAOJ as domestic partner and NASA and STFC (UK) as international partners. It is operated by these agencies in cooperation with ESA and NSC (Norway). CHIANTI is a collaborative project involving George Mason University, the University of Michigan (USA) and the University of Cambridge (UK).

## Appendix Assymmetric PSF Effects

Previous EIS analysis has indicated that it has an asymmetric point-spread function (PSF). EIS Software Note No. 8, available on the instrument website and distributed in SSW, reports that an asymmetric 2D Gaussian can fit the spatial distribution of the intensity of point source candidates in wide slit (slot) data. Young et al. (2012) argue that an elliptical PSF would explain systematic Doppler signatures observed in regions where there are strong intensity gradients, such as the solar limb or coronal bright points in coronal holes. A similar effect has been seen in the data from an earlier spectrometer (Haugen 1999).

An inclination of the spot image of a point source formed on the detector can lead to systematic Doppler signatures in the spectra. The spill over of photons along the inclination axis results in enhanced intensities on the blue or red side of the spectral line in pixels above and below the center of the spot. In regions where the intensities change slowly in space, the effect from pixel to pixel is small. This effect, however, can be important in the presence of very strong intensity gradients, where the spill over from brighter areas can skew the spectral line centroid measurements in the faint areas. The effect is simulated in the Software Note for the solar limb. Here we discuss its effect for this flare data set. Note that we focus on

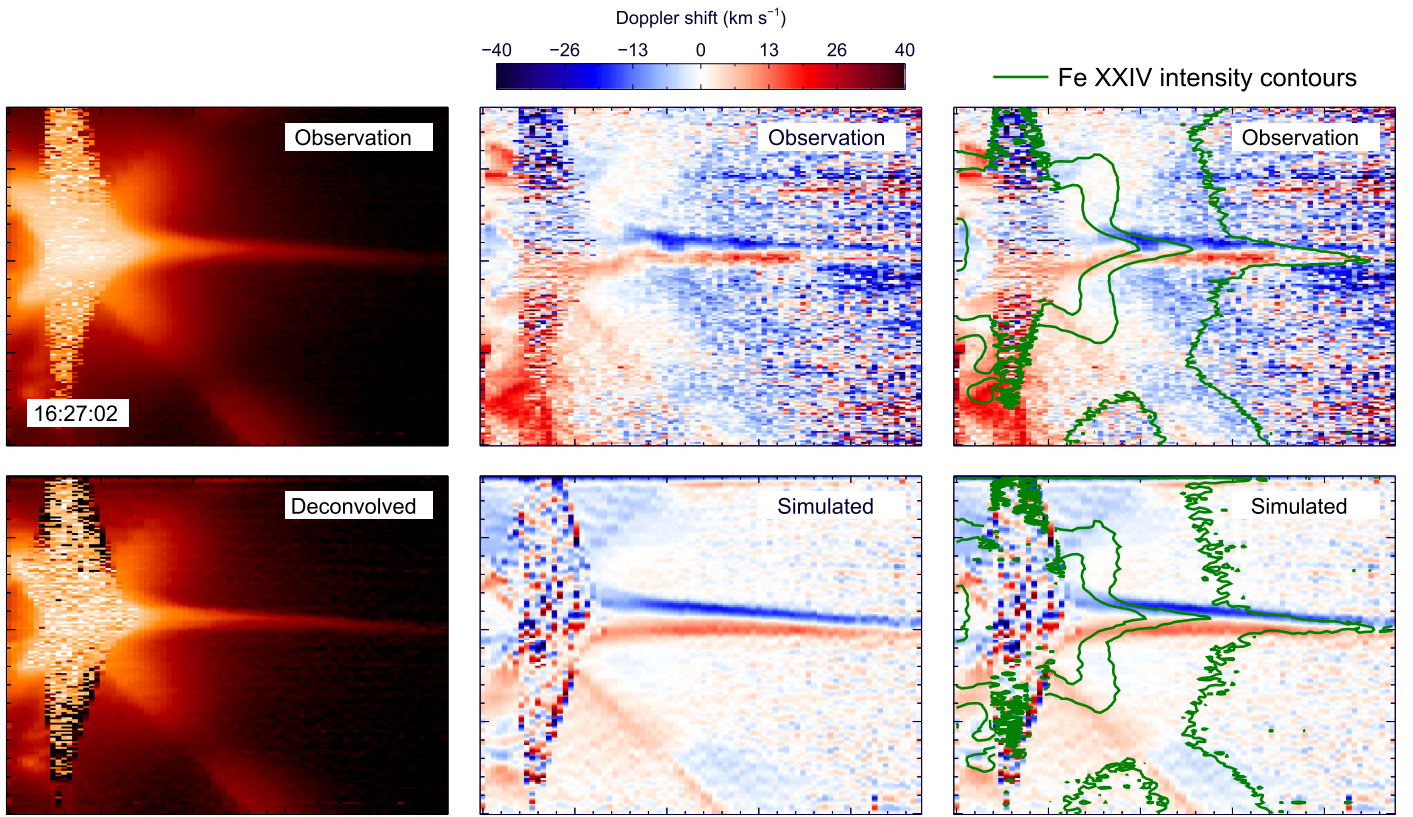


**Figure 12.** EIS observes unusual velocity signatures near the current sheet, but they appear to be artifacts of the instrument’s asymmetric PSF. Left panels: observed and deconvolved intensities for one of the Fe XXIV 192.04 Å rasters. These deconvolved intensities are used to create synthetic, zero velocity profiles that are convolved with the asymmetric PSF. Middle panels: observed and simulated velocity maps. The magnitude and spatial distribution of the simulated velocities are approximately consistent with the observations. Right panels: velocity maps with green intensity contours on top for reference.

the core of the PSF, which is relevant to the velocity signature. We have not addressed the diffracted signal from the mesh.

The current sheet in this event is a bright, elongated structure with strong intensity gradients perpendicular to its axis, and it is a likely region for this effect to be observed. The top row of Figure 12 shows the intensity (logarithmic scale) and Doppler velocity for one of the Fe XXIV 192.04 Å rasters. The 192.04 Å Doppler maps, which have not been presented before in the paper, all have a distinct red and blue Doppler pattern along the current sheet. If this were real, it would indicate systematic flows along the current sheet. As we will see, however, it appears to be an artifact of the asymmetric PSF.

The left panel in the bottom row shows an intensity map obtained from deconvolving the observed intensities using asymmetric Gaussian PSF [3″, 4″] and the AIA library routine `aia_deconvolve_richardsonlucy.pro`. We assume that this is the true distribution of the flare intensity that goes through the telescope aperture. In raster mode, every intensity column goes through the slit and gets dispersed on the detector to form a spectrum. We used this intensity to simulate a zero velocity spectrum centered at 192.04, assuming a thermal width at formation temperature of the line (18 MK), and an instrumental full width at half maximum of 2.5 EIS pixels (Lang et al. 2006). We then convolved the spectra with the asymmetric PSF to see the effect on the Doppler measurements. We fitted each spectra with single Gaussians and determined the centroids. The results are shown in the velocity map in the bottom-right panel, which presents the Doppler shift obtained from fitting the zero velocity spectra convolved with a PSF. A

comparison to the top panel reveals that systematic Doppler signatures that mimic the actual data can be introduced by the purely instrumental effect of an inclined PSF.

It may be possible to model and subtract this instrumental effect, perhaps revealing interesting velocity structure in the current sheet, but this is beyond the scope of the present paper. We explored a range of widths for the PSF of 2″–5″, and the results were comparable. We chose [3″, 4″] for display purposes because it is close to the values cited in work above, but we cannot yet conclude that it provides the best fit.

Finally, we have considered the impact of asymmetries in the PSF on the temperature ratio and width measurements. For these moments, the effects appear to be small.

### ORCID iDs

Harry P. Warren <https://orcid.org/0000-0001-6102-6851>  
David H. Brooks <https://orcid.org/0000-0002-2189-9313>  
Ignacio Ugarte-Urra <https://orcid.org/0000-0001-5503-0491>  
Jeffrey W. Reep <https://orcid.org/0000-0003-4739-1152>  
George A. Doschek <https://orcid.org/0000-0002-7625-9866>

### References

- Alexander, D., Harra-Murnion, L. K., Khan, J. I., & Matthews, S. A. 1998, *ApJL*, **494**, L235
- Antonucci, E., Gabriel, A. H., & Dennis, B. R. 1984, *ApJ*, **287**, 917
- Boerner, P., Edwards, C., Lemen, J., et al. 2012, *SoPh*, **275**, 41



- Boerner, P. F., Testa, P., Warren, H., Weber, M. A., & Schrijver, C. J. 2014, *SoPh*, **289**, 2377
- Brooks, D. H., Warren, H. P., & Ugarte-Urra, I. 2012, *ApJL*, **755**, L33
- Caspi, A., & Lin, R. P. 2010, *ApJL*, **725**, L161
- Chen, X., Liu, R., Deng, N., & Wang, H. 2017, *A&A*, **606**, A84
- Ciaravella, A., & Raymond, J. C. 2008, *ApJ*, **686**, 1372
- Ciaravella, A., Raymond, J. C., Li, J., et al. 2002, *ApJ*, **575**, 1116
- Culhane, J. L., Harra, L. K., James, A. M., et al. 2007, *SoPh*, **243**, 19
- Del Zanna, G. 2013, *A&A*, **555**, A47
- Del Zanna, G., Dere, K. P., Young, P. R., Landi, E., & Mason, H. E. 2015, *A&A*, **582**, A56
- Dere, K. P., Landi, E., Mason, H. E., Monsignori Fossi, B. C., & Young, P. R. 1997, *A&AS*, **125**, 149
- Doschek, G. A., Feldman, U., Kreplin, R. W., & Cohen, L. 1980, *ApJ*, **239**, 725
- Doschek, G. A., McKenzie, D. E., & Warren, H. P. 2014, *ApJ*, **788**, 26
- Doschek, G. A., & Warren, H. P. 2017, *ApJ*, **844**, 52
- Doschek, G. A., Warren, H. P., & Feldman, U. 2015, *ApJL*, **808**, L7
- Feldman, U., Mandelbaum, P., Seely, J. F., Doschek, G. A., & Gursky, H. 1992, *ApJS*, **81**, 387
- Forbes, T. G., & Acton, L. W. 1996, *ApJ*, **459**, 330
- Freeland, S. L., & Handy, B. N. 1998, *SoPh*, **182**, 497
- Garcia, H. A. 1994, *SoPh*, **154**, 275
- Golub, L., Deluca, E., Austin, G., et al. 2007, *SoPh*, **243**, 63
- Gou, T., Liu, R., & Wang, Y. 2015, *SoPh*, **290**, 2211
- Guidoni, S. E., & Longcope, D. W. 2011, *ApJ*, **730**, 90
- Guidoni, S. E., McKenzie, D. E., Longcope, D. W., Plowman, J. E., & Yoshimura, K. 2015, *ApJ*, **800**, 54
- Hannah, I. G., & Kontar, E. P. 2013, *A&A*, **553**, A10
- Hanneman, W. J., & Reeves, K. K. 2014, *ApJ*, **786**, 95
- Hara, H., Watanabe, T., Matsuzaki, K., et al. 2008, *PASJ*, **60**, 275
- Harra, L. K., Matthews, S. A., & Culhane, J. L. 2001, *ApJL*, **549**, L245
- Haugan, S. V. H. 1999, *SoPh*, **185**, 275
- Imada, S., Aoki, K., Hara, H., et al. 2013, *ApJL*, **776**, L11
- Kashyap, V., & Drake, J. J. 1998, *ApJ*, **503**, 450
- Kim, S., Shibasaki, K., Bain, H.-M., & Cho, K.-S. 2014, *ApJ*, **785**, 106
- Ko, Y.-K., Raymond, J. C., Lin, J., et al. 2003, *ApJ*, **594**, 1068
- Kohl, J. L., Esser, R., Gardner, L. D., et al. 1995, *SoPh*, **162**, 313
- Kosugi, T., Matsuzaki, K., Sakao, T., et al. 2007, *SoPh*, **243**, 3
- Laming, J. M. 2015, *LRSP*, **12**, 2
- Landi, E., Raymond, J. C., Miralles, M. P., & Hara, H. 2012, *ApJ*, **751**, 21
- Lang, J., Kent, B. J., Paustian, W., et al. 2006, *ApOpt*, **45**, 8689
- Lemen, J. R., Title, A. M., Akin, D. J., et al. 2012, *SoPh*, **275**, 17
- Li, L. P., Zhang, J., Su, J. T., & Liu, Y. 2016, *ApJL*, **829**, L33
- Lin, A. C., Nightingale, R. W., & Tarbell, T. D. 2001, *SoPh*, **198**, 385
- Liu, W., Chen, Q., & Petrosian, V. 2013, *ApJ*, **767**, 168
- Mariska, J. T., Doschek, G. A., & Bentley, R. D. 1993, *ApJ*, **419**, 418
- McKenzie, D. E., & Hudson, H. S. 1999, *ApJL*, **519**, L93
- O'Dwyer, B., Del Zanna, G., Mason, H. E., Weber, M. A., & Tripathi, D. 2010, *A&A*, **521**, A21
- Patsourakos, S., & Vourlidas, A. 2011, *A&A*, **525**, A27
- Poduval, B., DeForest, C. E., Schmelz, J. T., & Pathak, S. 2013, *ApJ*, **765**, 144
- Reeves, K. K., Freed, M. S., McKenzie, D. E., & Savage, S. L. 2017, *ApJ*, **836**, 55
- Reeves, K. K., & Golub, L. 2011, *ApJL*, **727**, L52
- Reeves, K. K., Guild, T. B., Hughes, W. J., et al. 2008a, *JGRA*, **113**, A00B02
- Reeves, K. K., Seaton, D. B., & Forbes, T. G. 2008b, *ApJ*, **675**, 868
- Savage, S. L., & McKenzie, D. E. 2011, *ApJ*, **730**, 98
- Savage, S. L., McKenzie, D. E., & Reeves, K. K. 2012, *ApJL*, **747**, L40
- Savage, S. L., McKenzie, D. E., Reeves, K. K., Forbes, T. G., & Longcope, D. W. 2010, *ApJ*, **722**, 329
- Schettino, G., Poletto, G., & Romoli, M. 2010, *ApJ*, **708**, 1135
- Scott, R. B., Longcope, D. W., & McKenzie, D. E. 2016, *ApJ*, **831**, 94
- Seaton, D. B., Bartz, A. E., & Darnel, J. M. 2017, *ApJ*, **835**, 139
- Shen, C., Reeves, K. K., Raymond, J. C., et al. 2013, *ApJ*, **773**, 110
- Shibata, K., Masuda, S., Shimojo, M., et al. 1995, *ApJL*, **451**, L83
- Tsuneta, S., Masuda, S., Kosugi, T., & Sato, J. 1997, *ApJ*, **478**, 787
- Warren, H. P. 2014, *ApJL*, **786**, L2
- Warren, H. P., Bookbinder, J. A., Forbes, T. G., et al. 1999, *ApJL*, **527**, L121
- Warren, H. P., & Brooks, D. H. 2009, *ApJ*, **700**, 762
- Warren, H. P., Ugarte-Urra, I., & Landi, E. 2014, *ApJS*, **213**, 11
- White, S. M., Thomas, R. J., & Schwartz, R. A. 2005, *SoPh*, **227**, 231
- Young, P. R., O'Dwyer, B., & Mason, H. E. 2012, *ApJ*, **744**, 14
- Zhu, C., Liu, R., Alexander, D., & McAteer, R. T. J. 2016, *ApJL*, **821**, L29
- Zweibel, E. G., & Yamada, M. 2009, *ARA&A*, **47**, 291